Nanowrinkled and Nanoporous Polyethylene Membranes Via Entanglement Arrangement Control

Hiroki Uehara, Takuya Tamura, Masaki Kakiage, and Takeshi Yamanobe*

Crystalline homopolymers, including polyethylene (PE), which has the simplest architecture, form a nanometer-sized combination of crystalline and amorphous components, but their arrangement control, similar to self-assembled phase-separation of block-copolymers, is usually difficult. However, molecular entanglements trapped between crystalline and amorphous components of homopolymers coincide with the segmental linking points on the interfaces of the microphase separation for block copolymers. Nanowrinkled PE membranes are prepared with a network of 30 nm-thick homogeneous lamellae using a novel entanglement control technique composed of biaxial melt-drawing and melt-shrinking procedures, which are limited for highly entangled ultrahigh molecular weight materials. Such a network arrangement of nanowrinkling lamellae spreading on membrane surface and also across the membrane thickness improves the mechanical properties of both tensile strength and tearing strength. Subsequent cold-drawing causes delamination of the lamellar interfaces, leading to the resultant nanoporous morphology composed of passing-through channels that are several tens of nanometers in diameter, without any solvent processing.

1. Introduction

Polymeric chains have two thermodynamically stable states that differ distinctly from each other. One is an entangled random coil, which is the amorphous component in the solid state. In contrast, folded or extended chains are aggregated as the crystalline component. The amorphous phase has higher entropy; thus, molecular orientation induced by various drawing techniques enables polymer crystallization. In turn, such crystalline chains become relaxed when melting into the amorphous phase. This means that these crystalline and amorphous phases exhibit thermodynamically reversible changes through orientation and relaxation of the molecular chains. Natural rubber is a good example, where the critical transition from the amorphous phase to the crystalline phase occurs during tensile drawing.[1] However, it is difficult to maintain the resultant oriented crystalline state because entropy recovery due to cross-linking points easily reverses it to the initial amorphous phase with the sample shrinkage.

Oriented crystallization from the rubbery amorphous state is achievable even for linear polyethylene (PE), which has the simplest molecular architecture but an ultrahigh molecular weight (UHMW) of over 10^6 Da.[2–10] Its higher melt viscosity enables ultradrawing, even above the melting temperature (T_m) due to the large number of entanglements contained. In contrast, such melt-drawing is impossible for conventional PE with a normal MW of 10^5 Da or lower. Melt-drawn UHMW-PE exhibits superior mechanical properties with resultant cylindrical extended-chain crystals (ECCs),[2–4,8] which completely differ from the transient crystallization during drawing of natural rubber.

Our previous studies[2–9] clarified that disentangling occurs during uniaxial melt-drawing of UHMW-PE. Indeed, the entanglement characteristics of UHMW-PE depend on the molding conditions[2,4] and the MW distribution of the material.[3,6,7,9] There are two types of entanglements: "shallow" entanglement, which is easily disentangled during drawing, and "deep" entanglement, which persists even after melt-drawing.[2] These types are distinguishable based on the relaxation time of molecular chains.[11] Rastogi et al.[12,13] claim that different entanglements located heterogeneously or homogeneously are formed during rapid or gradual heating of UHMW-PE materials in the melt. These analyses for molecular entanglements suggest that their amount and distribution can be changed by structural control with the melt-processing of UHMW-PE.

Solid-state relaxation after drawing of UHMW-PE also enables a control of molecular rearrangement, resulting in a periodic arrangement composed of lamellar crystals and amorphous layers.[14] Such ordered-phase morphology is quite similar to microphase separation of block copolymers.[15–21] Here, the former lamellar thickness of 30 nm coincides with the segmental length corresponding to the critical MW between entanglements (3600 Da) for PE,[22] which play a role similar to that of molecular linking points of the block copolymer chain, in terms of the boundary determining the phase separation (**Figure 1**). These molecular entanglements are trapped in the amorphous interface between folded chain crystal (FCC) lamellae; thus, UHMW-PE molecules cannot travel between

Prof. H. Uehara, T. Tamura, Dr. M. Kakiage,[+]
Prof. T. Yamanobe
Department of Chemistry and Chemical Biology
Gunma University
Kiryu, Gunma 376-8515, Japan
E-mail: hirokiuehara@gunma-u.ac.jp
[+] Present address: Department of Applied Chemistry
Saitama University, Sakura-ku, Saitama 338-8570, Japan

DOI: 10.1002/adfm.201102474

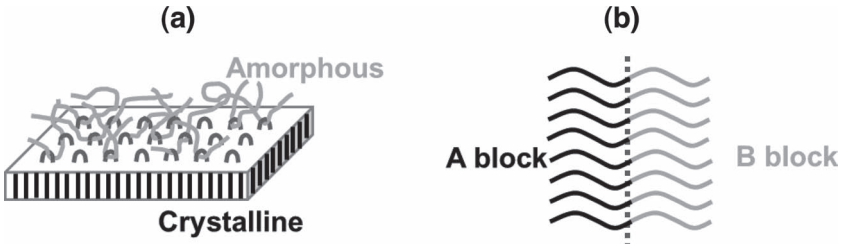

Figure 1. Comparison of crystalline-amorphous phase arrangements of homopolymer (a) and block copolymer (b). The phase boundaries between crystalline and amorphous components are determined by arrangements of entanglements for homopolymer (a) and linking points for block copolymer (b).

crystalline and amorphous phases on crystallization, possibly achieving an ordered lamellar morphology similar to that of block copolymer phase separation.

Here, it should be noted that characteristic morphologies of block copolymer are available for the preparation of functional materials. We have obtained bicontinuous networks of microphase separation for diblock copolymers containing both crystalline and amorphous segments by varying the crystallization conditions.[17,18,21] Further selective sulfonation or etching of amorphous components gave a electrolyte or nanoporous membrane supported by the surviving counter crystalline PE network. The former is advantageous for fuel applications because of its lower water uptake due to the restriction of excess water absorption induced by the crystalline PE backbone networks.[19] In contrast, the latter can be applied as an interface of an implantable glucose sensor, which requires excellent size selectivity for glucose permeation.[20]

In this study, the above-mentioned nanostructural controlling techniques of melt-drawing and subsequent relaxation were effectively combined for highly entangled UHMW-PE and further extended to biaxial drawing for an ideal homogeneous distribution of molecular entanglements. The resultant wide spread membrane consists of nano-ordered lamellar networks. This characteristic morphology was also applied for a template for a nanoporous membrane with a homogeneous arrangement of passing-through nanochannels.

2. Results and Discussion

Hizex million 340M UHMW-PE with a powder diameter of ≈150 μm and viscosity average MW of 3.5×10^6 was kindly supplied by Mitsui Chemical, Japan. This UHMW-PE powder was heated and compression molded at 180 °C into a film in vacuum, followed by slow cooling to room temperature. This molding temperature corresponds to the middle temperature between that resulting in shallow entanglements and that resulting in deep entanglements for this UHMW-PE material.[2,4] The averaging entanglement characteristic is preferred for verifying controllability of entanglement arrangements. Simultaneous biaxial-drawing was performed in both the vertical and the horizontal directions using a custom-made biaxial-drawing machine (**Figure 2**a) at 120 to 160 °C. A series of stress-strain curves recorded during biaxial drawing are compared in **Figure 3**a. Here, a series of curves obtained along the vertical direction are compared, but the data along the horizontal direction are the same as those along the vertical direction. Both drawings at 120 °C and 130 °C exhibit higher stresses due to solid-state deformation below the film T_m of 134 °C; however, drawing above 140 °C reduced stress to 0.5 MPa in the plateau region in the early stage of drawing. This stress value coincides with that for uniaxial melt-drawing of this UHMW-PE material,[2,5] indicating that this biaxial draw starts from a completely molten state. Our in situ X-ray measurements during uniaxial melt-drawing of UHMW-PE[5–7,9] revealed that molecular disentangling occurs within this plateau stress region. In contrast, later strain-hardening is attributed to orientation crystallization during melt-drawing.[2–7,9] In Figure 3a, biaxial melt-drawing above 150 °C prolongs the plateau stress region at 0.5 MPa near the end of the draw, corresponding to the vertical and horizontal strains of $5 \times 5 = 25$ at the maximum. This plateau region is much longer than that for uniaxial melt-drawing with a maximum strain of 10 for the same UHMW-PE material,[2,5] meaning that molecular disentanglement occurs more effectively for biaxial melt-drawing. This indicates that shallow entanglements almost disappear at these higher strains but deep entanglements still survive. At the higher temperature of 160 °C, melt-drawing of this UHMW-PE material was impossible both for uniaxial and biaxial melt-drawing.

Such a longer plateau region at 150 °C was suitable for preparing a series of membranes biaxially melt-drawn up to different draw ratios (*DR*). At the higher *DR* of 8×8, an ultrathin but wider membrane approximately 1 μm thick and with a 100×100 mm^2 area could be obtained (Figure 2b) depending on the dimensions of as-molded UHMW-PE film. The mechanical

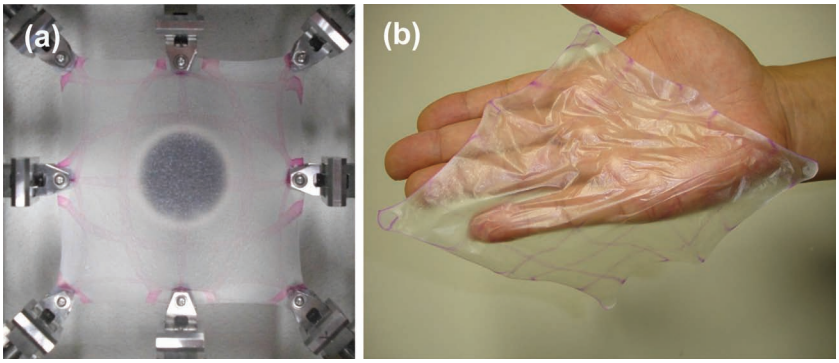

Figure 2. The biaxial drawing machine developed in this study (a) and a biaxially melt-drawn UHMW-PE membrane (b). Drawing was performed at 150 °C. Drawing stresses along both horizontal and vertical directions were recorded by load cells. Eight chucks were designed to grip the sample membrane with air compression, effectively preventing slipping due to the thinning membrane. The thickness of the resultant 8×8 membrane was approximate 1 μm in (b).

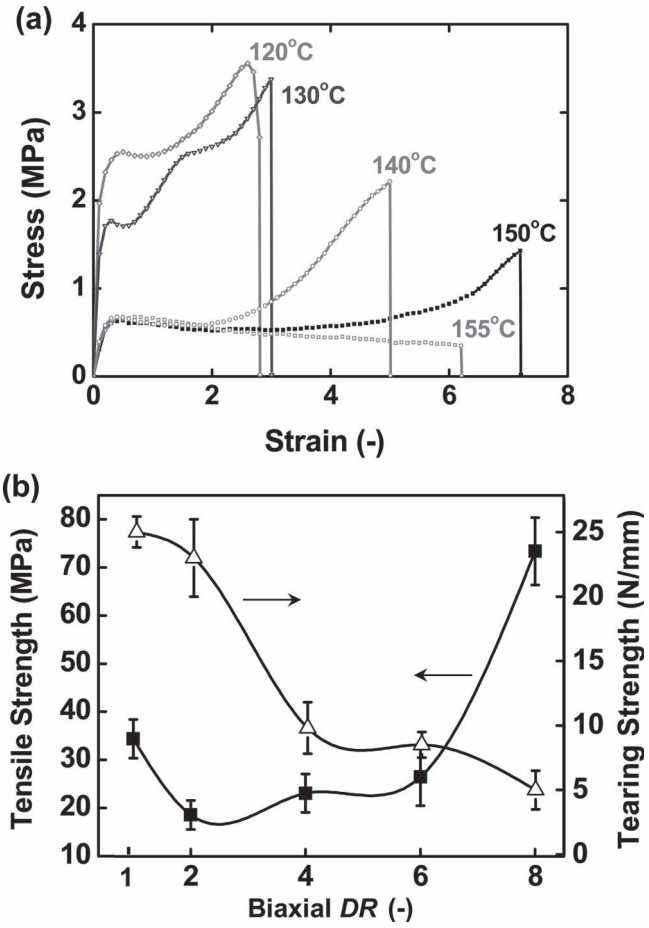

Figure 3. Drawing behavior and resultant mechanical properties of biaxially drawn UHMW-PE membranes. Stress-strain curves recorded during simultaneous biaxial drawing along vertical direction at the indicated temperatures are compared in (a). The same drawing stress was conformed along the horizontal direction in all cases. Resultant tensile (filled square) and tearing strengths (open triangle) were determined by tensile and tearing tests at room temperature in (b). Membranes with various *DR*s were prepared by biaxial melt-drawing at 150 °C.

properties of the biaxially melt-drawn membranes were evaluated by tensile and tearing tests for membranes with a thickness range of 5 to 125 μm for testing accuracy. The test specimens were cut into ribbons from the prepared membranes along the vertical direction. The tensile strength in Figure 3b gradually increases with biaxial *DR* from 2 × 2 to 6 × 6, followed by a rapid increase at the higher *DR*. At the biaxial *DR* of 8 × 8, the strength approaches twice that of the undrawn 1 × 1 film. In contrast, the tearing strength simultaneously decreases with biaxial *DR* to one fifth of that of the original film. It should be noted that both strength values for the sample specimens cut along the horizontal and diagonal directions were included in the error bars at the corresponding *DR*s even for different membrane thicknesses.

The origin of this inverse relationship between these membrane properties was interpreted with morphological observations. **Figure 4** depicts scanning electron microscopy (SEM) images of an initial as-molded film and a series of membranes with different biaxial *DR*s. The membrane surface morphologies at the lower *DR*s are composed of lamellar structures alone. In contrast, fibrillar structures are clearly observable beyond biaxial *DR*s of 4 × 4. The amount of latter fibrils increases with increasing biaxial *DR*s, but their orientation directions are completely random over the membrane surface, which is the reason that the mechanical properties in Figure 3 were independent of testing direction. Similar results are also confirmed from scanning probe microscopy (SPM) analyses. **Figure 5** shows SPM phase images of a series of membranes with different biaxial *DR*s. Here, a tapping mode was adopted to emphasize the difference between surface stiffness in crystalline components and that in amorphous components,[21] thus fibrillar structure was clearly recognized in the phase image, but the area between them was filled with lamellar structures, as revealed from the above SEM observation. A series of wide-angle X-ray diffraction (WAXD) and small-angle X-ray scattering (SAXS) images (Figure S1, Supporting Information) also exhibit random molecular orientation as well as random phase orientation of fibrillar ECCs and lamellar FCCs on the membrane flat surface. However, the membrane cross-section cleft by liquid nitrogen clearly exhibits a unique combination of fibrilar structures oriented along the membrane flat surface (lateral drawing direction) and lamellar structures arranged perpendicular (longitudinal) to the former structures (Figure 4d). This is well coincident with a shish-kebab morphology[23] combined with oriented ECCs and stacked FCCs obtained for uniaxial melt-drawing.[2–5,9,10,24] The former ECCs are formed during melt-drawing, but FCCs later crystallize epitaxially on the ECCs during sample cooling after melt-drawing.[5,9] Therefore, the molecules within FCCs usually align along the ECC chain axis, giving the perpendicular lamellar growth.

Such a combination of fibrillar ECCs and lamellar FCCs is also confirmed from the melting behavior for the resultant membranes prepared by biaxial melt-drawing. **Figure 6** compares the differential scanning calorimetry (DSC) endotherms for a series of membranes melt-drawn at 150 °C and the biaxial *DR*s ranging from 2 × 2 to 8 × 8. The double melting peaks are recorded at the lower T_m of 132–134 °C and the higher T_m beyond 150 °C, meaning that two different types of crystals coexist in the biaxially melt-drawn membranes. Similar double melting endotherms are also observable for uniaxially melt-drawn UHMW-PE.[2–4,8,10] Among these melting peaks, the lower one is observed for the undrawn UHMW-PE film, corresponding to the melting of usual FCCs with lamellar morphology.[2–4,8,10] In contrast, the higher T_m exceeds the equilibrium T_m of orthorhombic PE (145 °C),[25] which is often observed for commercial gel-spun UHMW-PE fibers constrained with wounding to a cupper piece sealed in a DSC pan.[26,27] For uniaxially drawn UHMW-PE fibers and films,[28–31] the higher temperature melting endotherm is attributed to the phase transition into hexagonal crystalline form. Indeed, the same phase transition, from orthorhombic to hexagonal form, was observable during heating for our biaxially melt-drawn 8 × 8 membrane, as revealed by in situ X-ray measurements during heating (not shown). This coincidence indicates that the fibrillar ECCs in Figure 4 are also constrained in the biaxially melt-drawn UHMW-PE membranes even without the above rigid sealing of the sample. However, a DSC heating scan of

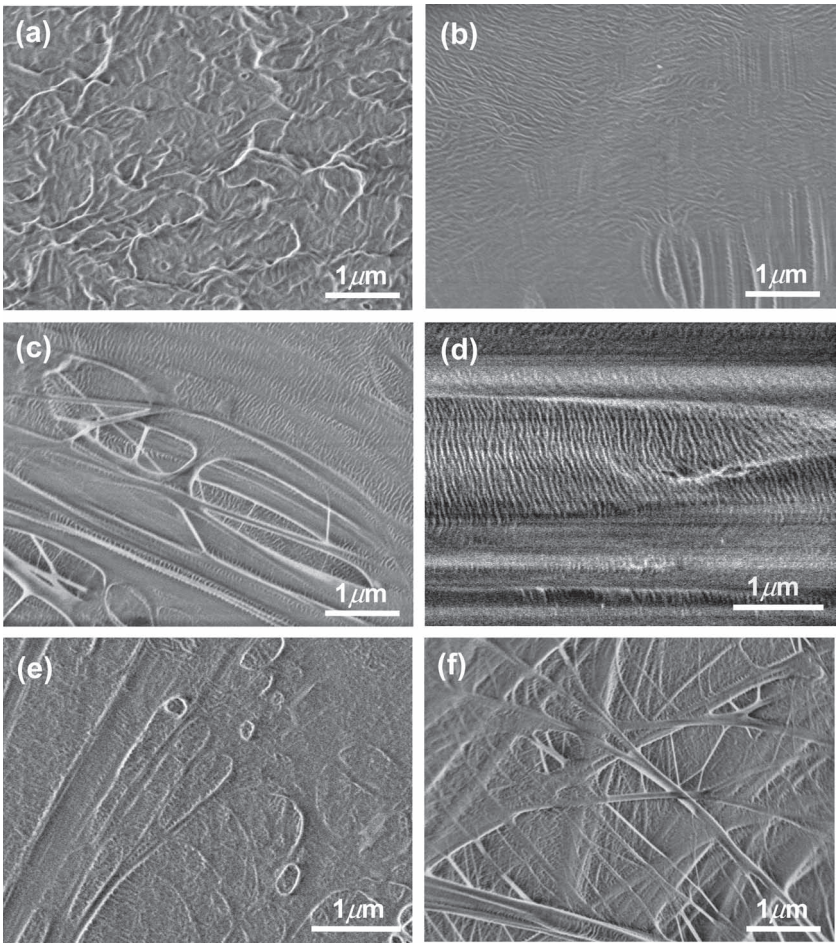

Figure 4. SEM images of original as-molded film (a) and membranes biaxially melt-drawn at 150 °C up to 2 × 2 (b), 4 × 4 (c, d), 6 × 6 (e), and 8 × 8 (f). These SEM images were acquired for the membrane surface (a–c,e,f), except for cross-section (d). Horizontal drawing directions in the biaxial membrane preparation were maintained for all images.

gel-spun UHMW-PE fibers always accompanies the melting of constrained ECCs at 150 °C with that of unconstrained ECCs around 145 °C because of stress distribution within the fiber bundles. In contrast, the latter melting was not observed in Figure 6. This suggests that homogeneous constraint is transmitted through random orientation of ECCs within the whole region of our biaxially melt-drawn membranes.

Here, the critical *DR* of 4 × 4 for the appearance of such a higher temperature melting endoderm is included in the plateau stress region for 150 °C drawing in Figure 3a. This implies that ECC formation is induced by molecular disentanglement during our biaxial melt-drawing. Correspondingly, the crystallinity estimated from the peak area of the melting endotherm (Figure S2, Supporting Information) rapidly increases from the biaxial *DR* of 4 × 4, which agrees well with the increase of tensile strength in Figure 3b. Susceptibility to tearing is induced by molecular anisotropy due to a weak van der Waals interaction between parallel molecules but strong coherent bonding along the chain direction. The gradual appearance of ECCs with biaxial melt-drawing develops tensile strength but reduces tearing strength, confirming that ECC is a key for determining these mechanical properties of the biaxially melt-drawn membrane prepared in this study. However, even at the highest *DR*, melting endotherms of both ECCs and FCCs are observed, suggesting that the resultant morphology is composed of a combination of these different crystalline structures.

DSC results in Figure 6 indicate that the lower *DR* membrane contains fewer ECCs because ECCs easily relax, melt, and disappear even if they form during biaxial drawing. In contrast, an increase in the number of ECCs at the higher *DR* prevents them from relaxing even when the draw is stopped. This result implies that tilting of the assembly composed of ECCs and FCCs for the higher *DR* membrane is induced by their relaxation before cooling, which is confirmable from a set of WAXD and SAXS analyses in Figure S1 (Supporting Information).

Thus, further positive relaxation was applied to introduce tilting and disappearances of ECCs, which may restrict the decrease in tearing strength even at higher *DR*s. For such structural relaxation of ECCs, shrinking treatment was applied while maintaining the molten state after biaxial melt-drawing. For instance, the as-prepared compression-molded film was biaxially drawn up to an initial *DR* of 7 × 7 at 150 °C, then shrunk to the latter *DR* of 4 × 4 and was annealed for 5 min while maintaining the latter *DR*. All these drawing, shrinking, and annealing treatments were conducted with the temperature maintained at 150 °C. Finally, specimens were rapidly cooled to room temperature. During these processes, any sample sag was fully avoidable. **Figure 7** compares the mechanical properties of the *DR* 4 × 4 membranes prepared by simple melt-drawing and subsequent shrinking from an initial *DR* 7 × 7, as described above. Both tensile strength and tearing strength double for the latter, confirming that the shrinking treatment is a key process for balancing tensile strength and tearing strength, which are usually in an opposing relationship. It should be noted that such larger melt-shrinking treatment is difficult for uniaxially melt-drawing of UHMW-PE, where the maximum shrinkage without sample sag or breaking for corresponding *DR* 7 × 7 = 49 is less than 20%. Homogeneous constraint within biaxially melt-drawn state could induce effective melt-shrinkage through prior ECCs spreading over the whole membrane.

Structural change induced by such shrinkage treatment is discussed next and membrane morphologies obtained before and after treatment are compared. **Figure 8** presents SEM images of the 4 × 4 membranes prepared by direct biaxial melt-drawing and melt-shrinking from the different *DR*s. The DSC melting profile for the resultant 4 × 4 membrane melt-shrunk from 7 × 7 is presented in Figure 6e. None of the fibrillar ECCs are observable in the SEM image of this melt-shrunk membrane (Figures 8a,b), but this membrane is composed of

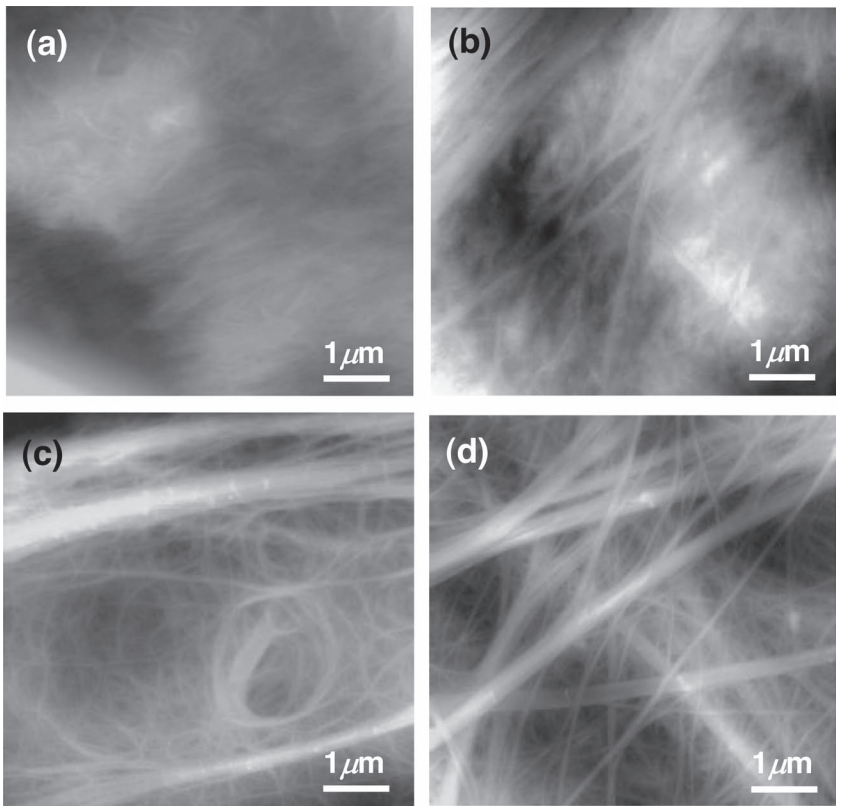

Figure 5. SPM phase images of membranes biaxially melt-drawn at 150 °C up to 2 × 2 (a), 4 × 4 (b), 6 × 6 (c), and 8 × 8 (d). Drawing directions were vertical and horizontal in these images. The tapping mode was adopted; thus, the extended fibrillar morphologies are emphasized in these images. These extended fibrils increase with increasing *DR*.

nanostructured networks of homogeneous FCC lamellae with a constant thickness of 30 nm. Such characteristic nanowrinkled morphology spreads over the entire membrane surface. Membrane cross-sections were also cleft in liquid nitrogen and observed. The direct melt-drawn membrane (Figure 4d) is composed of a shish-kebab structure combined with fibrillar ECCs along the membrane surface parallel to the drawing direction and lamellar FCC stacks are grown perpendicular to the former ECCs. In contrast, the shrunk membrane (Figure 8b) exhibits the network structure of lamellar FCCs with a constant thickness of 30 nm, which is the same nanowrinkled morphology as that of the membrane surface in Figure 8a. This result indicates that such homogeneous lamellar networks spread not only on the membrane surface but also across the thickness direction; thus, the applied stress is transmitted over the entire membrane without regional concentration, resulting in improved tensile strength and tearing strength. Correspondingly, the DSC melting endotherm for the shrunk membrane (Figure 6e) is sharper than those for both 4 × 4 and 7 × 7 membranes, indicating the homogeneity of lamellar thickness induced by above melt-shrinking treatment.

Such homogeneity of the resultant lamellar arrangement is also affected by shrinking *DR*. The 4 × 4 membrane melt-shrunk from 6 × 6 (Figure 8c) exhibits several flat marks ascribed to prior fibrillar ECCs. In contrast, such a mark completely disappears for the membrane melt-shrunk from 8 × 8 (Figure 8d). These results suggest that the larger shrinking effectively erase the ECCs and contribute to the homogeneous lamellar arrangements. However, the lamellar thickness is always 30 nm, independent of shrinking *DR*.

It is surprising that this critical lamellar thickness of 30 nm coincides with the length between molecular entanglements of PE.[22] As described above, the same critical value is obtained for the UHMW-PE film uniaxially drawn and subsequently relaxed in the solid state.[14] For a combination of biaxial melt-drawing and subsequent melt-shrinking in the present study, such homogeneous lamellar FCCs are formed on cooling after above sets of melt-drawing and melt-shrinking. UHMW-PE melt contains many molecular entanglements; thus, its melt viscosity is so high that a higher *DR* is obtained for melt-drawing. Similarly, large shrinking is also applicable even after the draw, which is impossible for solid-state drawing. This procedure contributes to the effective averaging of the positions of molecular entanglements, giving the resultant homogeneous lamellar arrangement.

The above nanowrinkled morphology is quite similar to the those obtained for uniaxial or biaxial orientation of the bilayered composite materials composed of hard metal

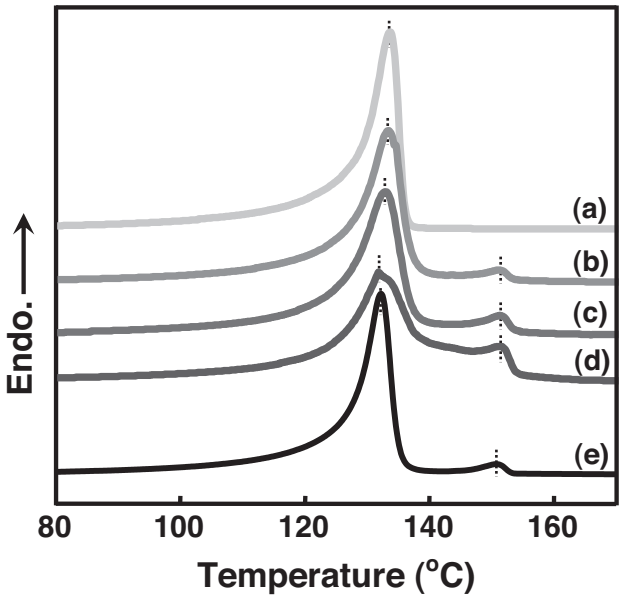

Figure 6. DSC thermograms recorded during heating from 80 to 170 °C at a scanning rate of 10 °C min^{-1}. Membranes were biaxially melt-drawn at 150 °C up to 2 × 2 (a), 4 × 4 (b), 6 × 6 (c), 8 × 8 (d), and resultant 4 × 4 shrank from 7 × 7 (e). All drawing and shrinking procedures were performed at 150 °C. The top positions of the peaks are indicated by dashed vertical lines.

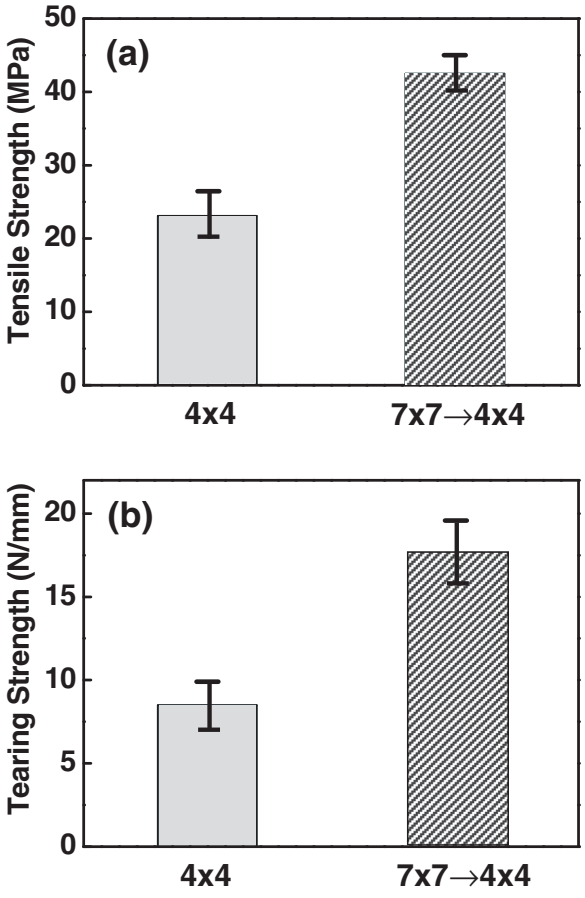

Figure 7. Effect of shrinking treatment on resultant mechanical properties. Tensile strength (a) and tearing strength (b) were compared at a biaxial *DR* of 4 × 4. The data for the direct melt-drawn membrane (left) were the same as in Figure 3b, but the resultant 4 × 4 membrane (right) was shrunk from 7 × 7. All drawing and shrinking procedures were performed at 150 °C; tensile and tearing tests were performed at room temperature.

or ceramics layer on soft polymer substrate.[32–37] A pioneering study performed by Bowen et al.[32] prepared the wrinkled metal thin layers on a rubbery amorphous poly(dimethyl siloxane) substrate. Stafford et al.[38–40] successfully applied this phenomenon for estimation of mechanical properties of surface layer of these composites. Yang et al.[34,36] has extended this wrinkling technique into biaxial orientation. Khine at al.[35] prepared the wrinkled metal arrays flowers by thermal shrinkage of the substrate polymer layer. However, the nanowrinkled lamellar arrangement for our membrane is much more minute on the nanometer scale. Indeed, the mechanism of nanowrinkling formation for our membranes is completely different. In the case of wrinkling for bilayered composites, the difference in the mechanical properties of these layers causes the periodic arrays. In contrast, the phase separation controlled by entanglement positioning gives the nanowrinkled lamellar arrangement for our biaxially melt-drawn and subsequent melt-shrunk UHMW-PE membrane. Therefore, the corresponding nanowrinkles spread within the internal of the membrane for our UHMW-PE membrane, resulting in the network arrangements. Another advantage of our technique for preparation of nanowrinkled surface lies in its simple melt-processing without the substrate adhesion or surface modification procedures.

The above nanowrinkled morphology composed of homogeneous lamellae can be interpreted as phase separation composed of crystalline and amorphous phases (Figure 1). A similar network-type phase separation is well known for the block copolymer system, as reviewed by Thomas et al.[15] Hillmyer et al.[16] reported that such nanostructured morphology of block copolymer is available for template of nanoporous polymeric materials. Russell et al.[41] previously reported that a combination of nanoporous thin membrane prepared from block copolymer phase separation and microporous substrate is available for filtration of small molecules. Lodge et al.[42] introduced a microemulsion technique, blending block copolymer and homopolymer for the preparation of network nanopores. As Phillips et al.[43] reported, chemical crosslinking of a selective continuous phase can give the robust nanoporous membrane. In particular, the bicontinuous morphology of block compolymer phase separation could be a template of network nanopores, which need not be aligned across the membrane.[44,45] However, these nanopore preparations from block copolymer precursor still require solvent and/or acid etching of counter block, which are often harmful for operation.

In this study, a non-solvent and non-etching procedure is attempted for the preparation of the nanoporous morphology using the nanowrinkled lamellar network composed of the crystalline phase and amorphous phase for our UHMW-PE membrane. Because the amorphous phase has lower mechanical strength than the crystalline phase, tensile deformation can destroy the amorphous phases, leading to the cavity. Therefore, tensile drawing was applied biaxially up to 2 × 2 in the solid state at 120 °C from a 4 × 4 membrane composed of homogeneous lamellar networks, resulting in a final *DR* of 8 × 8. For preparation of this nanoporous membrane, the 4 × 4 membrane was chosen because of the most typical homogeneous lamellar arrangement (Figure 8a,b), which was prepared by melt-shrinking treatment from *DR* 7 × 7. The obtained nanoporous morphology was analyzed by SEM and SPM images (**Figure 9**a–c). Many nanopores with a few tens of nanometers in diameter are clearly visible. The cross section image also reveals that these nanopores are interconnected across the membrane.

Porosity of such nanoporous membrane was verified by gas permeation tests (**Figure 10**). The oxygen gas permeation coefficient for this nanoporous UHMW-PE membrane with 30 μm thickness was 2.5×10^{-8} cm^3 (STP) cm/[cm^2 s cmHg]. In contrast, the commercial microporous UHMW-PE membrane (Hi-Pore, Asahi Kasei Chemical, 30 μm thick) with the larger pose sizes of a few hundreds of nanometers has an oxygen gas permeation coefficient of 1.8×10^{-9} cm^3 (STP) cm/[cm^2 s cmHg]. The above comparison suggests that our nanoporous membrane has superior permeation properties despite the smaller pore size. This indicates that the nanopore networks within our UHMW-PE membrane are passing-through due to the characteristic template morphology of the homogeneous lamellar networks. In contrast, the gas permeation coefficient of the starting nanowrinkled membrane (55 μm thick) is very low and similar to that for the undrawn membrane with 500 μm thickness.

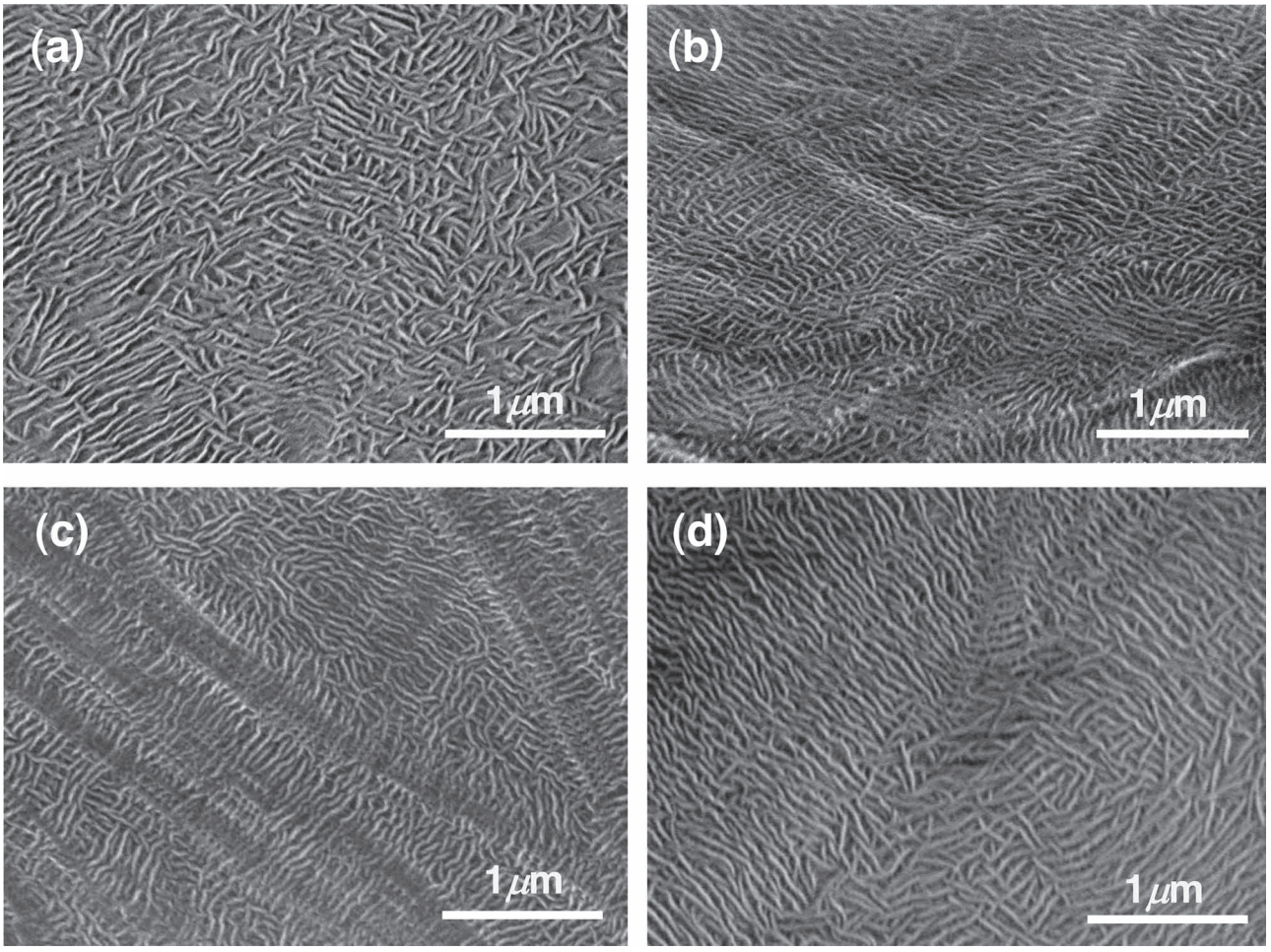

Figure 8. Nanowrinkled membrane morphologies for melt-shrunk up to 4 × 4 from different melt-drawn *DR*s. The top images exhibit the surface (a) and cross-section (b) morphologies biaxially melt-shrunk from initial melt-drawn *DR* of 7 × 7. The other surface morphologies of 4 × 4 membrane shrunk from initial 6 × 6 (c) or 8 × 8 (d) were also depicted in the bottom images. Both melt-drawing and melt-shrinking were performed at 150 °C. Horizontal drawing directions in the biaxial membrane preparation were maintained for all images. The top set corresponds to membrane (e) in Figure 6.

This means the nanowrinkled membrane with homogeneous lamellar arrangement is non-porous. This is preferable for the barrier layer for blocking various gas permeations. For example, its insert molding within a fuel tank, which is currently made by normal MW PE because of lighter weight for fuel efficiency, achieves one-composite composed of homopolymer PE alone for an ease of recycling but with hierarchical material design. Still, commercial PE fuel tanks require a nylon core layer to ensure the gasoline barrier, which prevents their effective recycling. Our UHMW-PE thin membrane can be an alternative of such a nylon core layer.

Commercial microporous UHMW-PE membranes for lithium ion battery separators have been manufactured by evaporating organic solvent (e.g., decaline) in the UHMW-PE gel for preparing membranes. Such use of organic solvent in membrane processing endangers manufacturing operators and requires the cost of collecting and recycling the used solvent to minimize environmental release. In contrast, our manufacturing protocol for a nanoporous UHMW-PE membrane is environmental friendly and safe because it does not require solvent dissolution or chemical etching. The lack of residual solvent and the high strength of our UHMW-PE membranes are also advantageous for environmental and medical support materials, including cleaning filters for water purification or artificial dialyzers. However, the precise estimations of pore size and porosity of the membrane are required for full understanding the characteristics of our nanoporous UHMW-PE membranes, which should be examined in a future study.

Another attempt was made for orientation of the nanowrinkled lamellar morphologies obtained in this study. The melt-shrinking was performed to different vertical and horizontal *DR*s of 4 × 5 from initial 7 × 7 (Figure 9d). The resultant homogeneous lamellae align along the vertical direction. This lamellar alignment is similar to wrinkled morphologies obtained by uniaxial deformation of the bilayered composites,[32–40] but the alignment direction is perpendicular, i.e., orientated to the larger shrinking direction. This is because the origin of our homogeneous lamellae is attributed to the residual ECCs

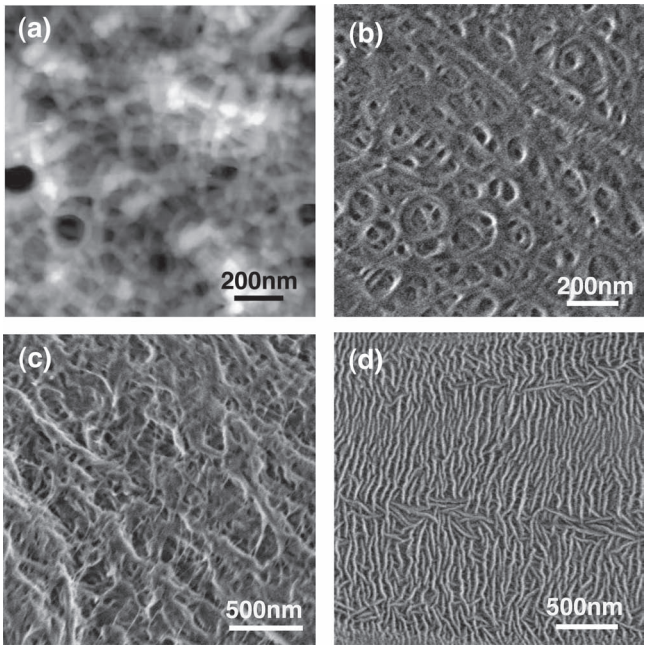

Figure 9. Nanoporous morphology and aligned nanowrinkles of UHMW-PE membranes prepared in this study. Nanoporous membrane surface was compared by SPM (a) and SEM (b) images. The nanoporous membrane was prepared by biaxial solid-drawing at 120 °C up to the final *DR* of 8 × 8 from initial 4 × 4. The initial 4 × 4 membrane was prepared by prior melt-drawing up to 7 × 7, followed by subsequent melt-shrinking to 4 × 4. The SEM image (c) was edge-viewed for the cross section of the nanoporous membrane cleft in liquid nitrogen. In contrast, the aligned nanowrinkling surface was obtained for 4 × 5 membrane prepared by changing the horizontal and vertical melt-shrinking *DR*s (d).

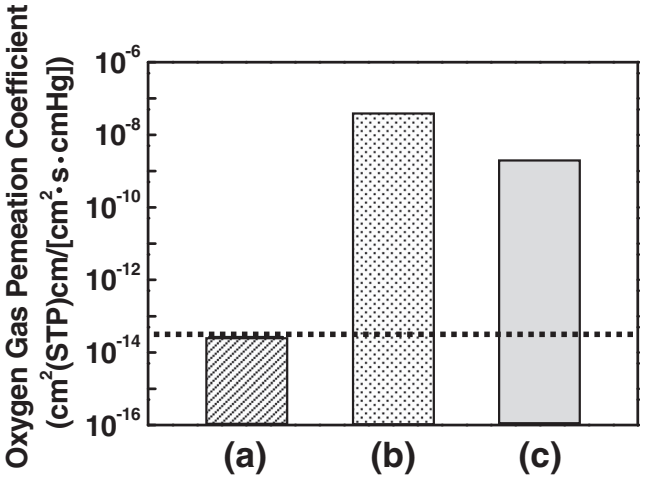

Figure 10. Oxygen gas permeation coefficient of nanowrinkled and nanoporous UHMW-PE membranes. The nanowrinkled membrane (a) was prepared by melt-shrinking up to 4 × 4 from initially melt-drawn *DR* of 7 × 7, which is same as shown in Figure 8a,b. The nanoporous membrane (b) was prepared by biaxial solid-drawing up to 8 × 8 from the nanowrinkled membrane, which is same as shown in Figure 9a,b. For comparison, the commercial lithium-ion battery separator of microporous UHMW-PE membrane (c) was also tested. The dotted line indicates the value for the initial undrawn UHMW-PE membrane. The thicknesses of these membranes are summarized in Table S1 (Supporting Information).

along the horizontal direction with lower shrinking, which can be nuclei for FCC formation along the perpendicular direction on cooling from melt-processing. Very recently, Keller et al.[46] investigated the protein assembly on the stacked FCC surfaces prepared by uniaxial melt-drawing of UHMW-PE, therefore if our nanowrinkled surface composed of FCC networks may control such protein absorption or assembly, it is also applicable for protein nanopatterning.

Thus far, the molecular entangling of polymeric chains is considered a negative characteristic that restricts crystallization, resulting in inferior physical properties. However, our melt-drawing and subsequent melt-shrinking techniques could successfully control the entanglement positions of UHMW-PE, giving the resultant homogeneous lamellar morphology. Such entanglement control enables preparing nanowrinkled or nanoporous, but large-area, membranes even from PE homopolymer.

3. Conclusions

Highly entangled UHMW-PE films could be biaxially melt-drawn and subsequently melt-shrunk into ultrathin but wider membranes with thickness lower than 5 μm and area of over 100 × 100 mm^2. Nanowrinkled morphology composed of the homogeneous lamellar networks spread both on the membrane surface and across the thickness of the prepared UHMW-PE membranes. Such nanostructural formation of crystalline/amorphous phases is induced by homogeneous entanglement positioning controlled by our novel melt-processing technology, giving the improvement of the mechanical properties of the membrane. Additional solid-state tensile drawing can separate lamellar boundaries, resulting in nanoporous UHMW-PE membrane. This preparation protocol for nanoporpus membranes does not contain solvent or an acid etching procedure, which are necessary for preparation of nanoporous membranes from block copolymer precursors. Also, the pore size of our nanoporous membrane is 1/10 of the commercial lithium-ion battery separator even though both were made from UHMW-PE materials.

4. Experimental Section

Film preparation: UHMW-PE used was Hizex 340M supplied by Mitsui Chemical. The UHMW-PE powder was sandwiched between commercial polyimide films (UPILEX-125S, Ube) and compression molded into the film at 180 °C and 5 MPa for 10 min in vacuum, followed by slow cooling to room temperature. A press machine equipped with a vacuum chamber (Boldwin, Japan) was used. The resultant film was 80 to 800 μm thick as standards.

Biaxial drawing: The above-prepared UHMW-PE films were biaxially drawn at 120 to 160 °C and a cross-head speed (CHS) of 5 mm min^{-1} along vertical and horizontal directions up to a *DR* of 2 × 2 to 8 × 8. A custom-made machine (Figure 1a) was designed for such biaxial drawing. The sample membrane was gripped by eight chucks with air-compression control to prevent slippage due to the membrane thinning during drawing. Drawing stresses along the vertical and horizontal directions were recorded using load cells (LUR-A-50NSA1, Kyowa Electronic Instruments, Japan). Depending on the targeted *DR*s, the initial sample films were cut to 20 × 20 to 40 × 40 mm^2.

Measurements: The mechanical properties of the prepared membranes were measured by a Tensilon RTC-1325A tensile tester (A&D, Japan) at room temperature. Strips 5 mm or 25 mm wide and 50 mm long were cut from the prepared membranes for tensile or tearing tests. Tensile tests were performed at a CHS of 20 mm min^{-1} for 30 mm gauge length. Tensile strength was calculated from the maximum recorded stress at the breaking point, and the tensile modulus was evaluated from the slope of the stress–strain curves. Tearing tests were conducted at a CHS of 200 mm min^{-1} when the initial notch, 10 mm long, was made at the center of strips that were 25 mm wide and 30 mm long. Two ends of the strips at the top side were turn in up and down directions and clamped. Tearing strength was defined as the maximum recorded stress divided by the membrane thickness.

Morphologies of the resultant membranes were observed using a Hitachi field-emission SEM S-4800 operated at 1.0 kV. SPM observation was performed with an E-sweep module controlled by a NanoNavi system (SII NanoTechnology, Japan). Continuous right-to-left and left-to-right scans within a 5 μm square were made in a tapping mode with a scan speed of 1 H z. The sample membranes were uncoated for both SPM and SEM morphological observations, so any artifacts were negligible.

A Perkin-Elmer Diamond DSC was used for DSC measurements. Heating scans were performed from 50 to 180 °C at a rate of 10 °C min^{-1} under a nitrogen gas flow. The sample T_m was evaluated as the peak temperature of the melting endotherm. The temperature and fusion heat were calibrated using indium and tin standards. To avoid the effects of both shrinking stress of the oriented membrane on melting and delay in heat transfer during a heating scan, a small amount of silicone oil was placed between the sample and the bottom of the DSC sample pan.

The gas permeation of the prepared UHMW-PE membranes was analyzed with oxygen using a K-315N gas permeation analyzer (Tsukuba-Rikaseiki, Japan). The membrane area for permeation measurement was 30 mm in diameter.

Supporting Information

Supporting Information is available from the Wiley Online Library or from the author.

Acknowledgements

This work was financially supported by the Industrial Technology Research Grant Program from the New Energy and Industrial Technology Development Organization (NEDO) of Japan and the Kurita Water and Environment Foundation.

Received: October 14, 2011
Revised: December 30, 2011
Published online: March 7, 2012

[1] S. Murakami, K. Senoo, S. Toki, S. Kohjiya, *Polymer* **2002**, *43*, 2117.
[2] H. Uehara, M. Nakae, T. Kanamoto, A. E. Zachariades, R. S. Porter, *Macromolecules* **1999**, *32*, 2761.
[3] M. Nakae, H. Uehara, T. Kanamoto, T. Ohama, R. S. Porter, *J. Polym. Sci., Polym. Phys. Ed.* **1999**, *37*, 1921.
[4] M. Nakae, H. Uehara, T. Kanamoto, A. E. Zachariades, R. S. Porter, *Macromolecules* **2000**, *33*, 2632.
[5] H. Uehara, M. Kakiage, T. Yamanobe, T. Komoto, S. Murakami, *Macromol. Rapid Commun.* **2006**, *27*, 966.
[6] M. Kakiage, T. Yamanobe, T. Komoto, S. Murakami, H. Uehara, *J. Polym. Sci., Polym. Phys. Ed.* **2006**, *44*, 2455.
[7] M. Kakiage, T. Yamanobe, T. Komoto, S. Murakami, H. Uehara, *Polymer* **2006**, *47*, 8053.
[8] H. Uehara, R. Yoshida, M. Kakiage, T. Yamanobe, T. Komoto, *Ind. Eng. Chem. Res.* **2006**, *45*, 7801.
[9] M. Kakiage, M. Sekiya, T. Yamanobe, T. Komoto, S. Sasaki, S. Murakami, H. Uehara, *Polymer* **2007**, *48*, 7385.
[10] M. Kakiage, M. Sekiya, T. Yamanobe, T. Komoto, S. Sasaki, S. Murakami, H. Uehara, *J. Phys. Chem. B* **2008**, *112*, 5311.
[11] M. Kakiage, H. Uehara, T. Yamanobe, *Macromol. Rapid Commun.* **2008**, *29*, 1571.
[12] S. Rastogi, D. R. Lippits, G. W. M. Peters, R. Graf, Y. Yao, H. W. Spiess, *Nat. Mater.* **2005**, *4*, 635.
[13] A. Pandey, Y. Champouret, S. Rastogi, *Macromolecules* **2011**, *44*, 4952.
[14] H. Uehara, K. Takeuchi, M. Kakiage, T. Yamanobe, T. Komoto, *Macromolecules* **2007**, *40*, 5820.
[15] C. Park, J. Yoon, E. L. Thomas, *Polymer* **2003**, *44*, 6725.
[16] D. A. Olson, L. Chen, M. A. Hillmyer, *Chem. Mater.* **2008**, *20*, 869.
[17] H. Uehara, T. Yoshida, M. Kakiage, T. Yamanobe, T. Komoto, *J. Polym. Sci., Polym. Phys. Ed.* **2006**, *44*, 1731.
[18] H. Uehara, T. Yoshida, M. Kakiage, T. Yamanobe, T. Komoto, K. Nomura, K. Nakajima, M. Matsuda, *Macromolecules* **2006**, *39*, 3971.
[19] H. Uehara, M. Kakiage, M. Sekiya, T. Yamagishi, T. Yamanobe, K. Nakajima, T. Watanabe, K. Nomura, K. Hase, M. Matsuda, *Macromolecules* **2009**, *42*, 7627.
[20] H. Uehara, M. Kakiage, M. Sekiya, D. Sakuma, T. Yamanobe, N. Takano, A. Barraud, E. Meurville, P. Ryser, *ACS Nano* **2009**, *3*, 924.
[21] H. Uehara, Y. Karaki, S. Wada, T. Yamanobe, *ACS Appl. Mater. Interfaces* **2010**, *2*, 2707.
[22] W. W. Graessley, *Adv. Polym. Sci.* **1974**, *16*, 1.
[23] Z. Bashir, A. Keller, *Colloid Polym. Sci.* **1989**, *267*, 116.
[24] K. D. Jandt, M. Buhk, M. J. Miles, J. Pertermann, *Polymer* **1994**, *35*, 2458.
[25] F. A. Quinn Jr., L. Mandelkern, *J. Am. Chem. Soc.* **1958**, *80*, 3178.
[26] P. J. Lemstra, N. A. J. M. van Aerle, C. W. M. Bastiaansen, *Polym. J.* **1987**, *19*, 85.
[27] S. Tsubakihara, A. Nakamura, M. Yasuniwa, *Polym. J.* **1996**, *28*, 489.
[28] N. A. J. M. van Aerle, P. J. Lemstra, A. W. M. Braam, *Polym. Commun.* **1989**, *30*, 7.
[29] H. Uehara, T. Kanamoto, A. Kawaguchi, S. Murakami, *Macromolecules* **1996**, *29*, 1540.
[30] K. Tashiro, S. Sasaki, M. Kobayashi, *Macromolecules* **1996**, *29*, 7460.
[31] M. Kakiage, T. Tamura, S. Murakami, H. Takahashi, T. Yamanobe, H. Uehara, *J. Mater. Sci.* **2010**, *45*, 2574.
[32] N. Bowden, S. Brittain, A. G. Evans, J. W. Hutchinson, G. M. Whitesides, *Nature* **1998**, *393*, 146.
[33] S. P. Lacour, S. Wagner, Z. Huang, Z. Sau, *Appl. Phys. Lett.* **2003**, *82*, 2404.
[34] P.-C. Lin, S. Yang, *Appl. Phys. Lett.* **2007**, *90*, 241903.
[35] C.-C. Fu, A. Grimes, M. Long, C. G. L. Ferri, B. D. Rich, S. Ghosh, L. P. Lee, A. Gopinathan, M. Khine, *Adv. Mater.* **2009**, *21*, 4472.
[36] S. Yang, K. Khare, P.-C. Lin, *Adv. Funct. Mater.* **2010**, *20*, 2550–2564.
[37] L. Zhang, X. Lang, A. Hirata, M. Chen, *ACS Nano* **2011**, *5*, 4407.
[38] C. M. Stafford, C. Harrison, K. L. Beers, A. Karim, E. J. Amis, M. R. Van Landingham, H.-C. Kim, W. Volksen, R. D. Miller, E. E. Simonyi, *Nat. Mater.* **2004**, *3*, 545.

[39] J. Y. Chung, J.-H. Lee, K. L. Beers, C. M. Stafford, *Nano Lett.* **2011**, *11*, 3361.
[40] E. P. Chan, S. Kundu, Q. Lin, C. M. Stafford, *ACS Appl. Mater. Interfaces* **2011**, *3*, 331.
[41] S. Y. Yong, I. Ryu, H. Y. Kim, J. K. Kim, S. K. Jang, T. P. Russell, *Adv. Mater.* **2006**, *18*, 709.
[42] N. Zhou, F. S. Bates, T. P. Lodge, *Nano Lett.* **2006**, *6*, 2354.
[43] W. A. Phillip, M. Amendt, B. O'Neill, L. Chen, M. A. Hillmyer, E. L. Cussler, *ACS Appl. Mater. Interfaces* **2009**, *1*, 472.
[44] K.-V. Peinemann, V. Abetz, P. F. W. Simon, *Nat. Mater.* **2007**, *6*, 992.
[45] D. L. Gin, R. D. Noble, *Science* **2011**, *332*, 674.
[46] T. F. Keller, J. Schönfelder, J. Reichert, N. Tuccitto, A. Licciardello, G. M. L. Messina, G. Merlett, K. D. Jandt, *ACS Nano* **2011**, *5*, 3120.